Monthly Notices
of the
ROYAL ASTRONOMICAL SOCIETY

MNRAS **482,** 5553–5566 (2019) doi:10.1093/mnras/sty3036

Detection of a giant flare displaying quasi-periodic pulsations from a pre-main-sequence M star by the Next Generation Transit Survey

James A. G. Jackman,[1,2]★ Peter J. Wheatley,[1,2] Chloe E. Pugh,[1,2] Dmitrii Y. Kolotkov,[1,2] Anne-Marie Broomhall,[1,2,3] Grant M. Kennedy,[1,2] Simon J. Murphy,[4] Roberto Raddi,[1,2,5] Matthew R. Burleigh,[6] Sarah L. Casewell,[6] Philipp Eigmüller,[7,8] Edward Gillen,[9] Maximilian N. Günther,[9] James S. Jenkins,[10] Tom Louden,[1,2] James McCormac,[1,2] Liam Raynard,[6] Katja Poppenhaeger,[11] Stéphane Udry,[12] Christopher A. Watson[11] and Richard G. West[1,2]

[1]*Department of Physics, University of Warwick, Gibbet Hill Road, Coventry CV4 7AL*
[2]*Centre for Exoplanets and Habitability, University of Warwick, Gibbet Hill Road, Coventry CV4 7AL*
[3]*Institute of Advanced Studies, University of Warwick, Coventry CV4 7HS*
[4]*School of Physical, Environmental and Mathematical Sciences, University of New South Wales Canberra, ACT 2612, Australia*
[5]*Dr. Remeis-Sternwarte, Friedrich Alexander Universität Erlangen-Nürnberg, Sternwartstr. 7, 96049 Bamberg, Germany*
[6]*Department of Physics and Astronomy, Leicester Institute of Space and Earth Observation, University of Leicester, University Road, Leicester LE1 7RH*
[7]*Institute of Planetary Research, German Aerospace Center, Rutherfordstrasse 2, 12489 Berlin, Germany*
[8]*Center for Astronomy and Astrophysics, TU Berlin, Hardenbergstr. 36, D-10623 Berlin, Germany*
[9]*Astrophysics Group, Cavendish Laboratory, J.J. Thomson Avenue, Cambridge CB3 0HE*
[10]*Departamento de Astronomia, Universidad de Chile, Casilla 36-D, Santiago, Chile*
[11]*Astrophysics Research Centre, Queen's University of Belfast, 1 University Road, Belfast BT7 1NN*
[12]*Department of Astronomy of the University of Geneva, Observatoire de Genéve, 51 ch des Maillettes, 1290 Versoix, Switzerland*

Accepted 2018 November 5. Received 2018 November 5; in original form 2018 September 25

ABSTRACT

We present the detection of an energetic flare on the pre-main-sequence M3 star NGTS J121939.5–355557, which we estimate to be only 2 Myr old. The flare had an energy of $3.2 \pm^{0.4}_{0.3} \times 10^{36}$ erg and a fractional amplitude of 7.2 ± 0.8, making it one of the most energetic flares seen on an M star. The star is also X-ray active, in the saturated regime with $\log L_X/L_{Bol} = -3.1$. In the flare's peak, we have identified multimode quasi-periodic pulsations formed of two statistically significant periods of approximately 320 and 660 s. This flare is one of the largest amplitude events to exhibit such pulsations. The shorter period mode is observed to start after a short-lived spike in flux lasting around 30 s, which would not have been resolved in *Kepler* or *TESS* short-cadence modes. Our data show how the high cadence of the Next Generation Transient Survey (NGTS) can be used to apply solar techniques to stellar flares and to identify potential causes of the observed oscillations. We also discuss the implications of this flare for the habitability of planets around M star hosts and how NGTS can help our understanding of this.

Key words: stars: flare – stars: individual: NGTS J121939.5–355557 – stars: low-mass – stars: pre-main-sequence.

1 INTRODUCTION

Stellar flares from M stars provide some of the most dramatic stellar events, yet they cannot be predicted beforehand. Catching the relatively rare high-energy events therefore requires long-duration measurements of many stars, such as those from wide-field surveys for transiting exoplanets. The energies output in such events often dwarf the largest seen from the Sun (10^{32} erg for the Carrington Event; Carrington 1859; Tsurutani et al. 2003) and the flares themselves can be seen over a wide range of wavelengths, notably in optical, ultraviolet (UV) and X-rays. The high-energy irradiation provided by these flares, combined with the discoveries of habitable zone exoplanetary systems, has in recent years

★ E-mail: J.Jackman@warwick.ac.uk

provoked discussion of the role of flares in habitability. Along with a range of detrimental effects, such as ozone depletion (Segura et al. 2010) and potential atmospheric loss (e.g. Lammer et al. 2007), stellar flares have been invoked as a possible way of providing the near-ultraviolet flux required for prebiotic chemistry on M dwarf exoplanetary systems (e.g. Ranjan, Wordsworth & Sasselov 2017; Rimmer et al. 2018). In order to determine the role of stellar flares in exoplanetary habitability, it is necessary to observe not only the more common lower-energy events but also the rarest high-energy events, and also to track how the occurrence of such events varies with stellar age.

When observed in the optical, the highest-energy white-light flares from mid-M type and later spectral types can change the brightness of the star by magnitudes for hours before returning to quiescence (e.g. Gizis et al. 2017; Paudel et al. 2018). The largest amplitude events can also make stars that normally reside below the sensitivity of a survey visible for short periods of time (e.g. the $\Delta V < -11$ flare from ASASSN-16ae identified by Schmidt et al. 2016). These flares provide evidence that strong magnetic activity is present on stars well past the fully convective boundary of M3–M4. This boundary marks where stellar interiors no longer contain a radiative zone and magnetic fields are generated by an alternative dynamo mechanism to earlier spectral types (e.g. Houdebine & Mullan 2015; Houdebine et al. 2017). While rare for individual stars, surveys with large fields of view can make regular detections of these high-amplitude events. In recent years, such flares have even been identified as a potential 'fog' for future large-scale surveys such as the Large Synoptic Survey Telescope (LSST), because of their ability to mimic other astrophysical transient events (e.g. Kulkarni & Rau 2006; Berger et al. 2012, 2013).

Some large-amplitude stellar flares have exhibited complex substructure. One type of substructure consists of the oscillations of flare intensity with time, commonly referred to as quasi-periodic pulsations (QPPs). A common phenomenon on the Sun (Kupriyanova et al. 2010; Simões, Hudson & Fletcher 2015; Inglis et al. 2016), QPPs remain relatively rare in observations of stellar flares. Those that have been observed have been seen in the optical (e.g. Balona et al. 2015), microwave (Zaitsev et al. 2004), UV (Welsh et al. 2006; Doyle et al. 2018) and X-ray (Mitra-Kraev et al. 2005; Pandey & Srivastava 2009; Cho et al. 2016).

The exact cause of these pulsations is not yet known. However, numerous mechanisms have been proposed and it is indeed possible that different mechanisms act in different cases. These mechanisms can be split into two groups: those where the flare emission is modulated by magnetohydrodynamic (MHD) oscillations, and those based on some regime of repetitive magnetic reconnection (Nakariakov et al. 2016). In the first case, MHD oscillations can directly affect the flare emission by modulating the plasma parameters (e.g. Nakariakov & Melnikov 2009a); for example, variations of the magnetic field strength would cause gyrosynchrotron emission to vary. In addition, the oscillations could indirectly affect the emission by modulating the kinematics of charged particles in the flaring coronal loops, which in turn would cause bremsstrahlung emission at the footpoints to appear periodically (e.g. Zaitsev & Stepanov 2008). In the second case, the repetitive reconnection could be the result of external triggering, for example, by leakage of MHD oscillations of a nearby structure (Nakariakov et al. 2006). Alternatively, it could result from a 'magnetic dripping' mechanism, which does not require an external trigger (e.g. McLaughlin et al. 2018). For this scenario, magnetic reconnection occurs only when some threshold energy is reached. This reconnection then releases energy and the process repeats periodically. Examples of this regime are reported by Murray, van Driel-Gesztelyi & Baker (2009), McLaughlin, Thurgood & MacTaggart (2012) and Thurgood, Pontin & McLaughlin (2017). If the mechanism behind a particular observation of QPPs in a flare can be determined, then it might be possible to estimate coronal plasma parameters in the vicinity of the flare via coronal seismology (e.g. Van Doorsselaere, Kupriyanova & Yuan 2016).

The time-scale of QPPs can range from milliseconds to minutes (e.g. McLaughlin et al. 2018) and, as a result, without observations of a similar or higher cadence these short-lived behaviours will be missed. For solar flares, this cadence is regularly achieved (e.g. Dolla et al. 2012; Kumar, Nakariakov & Cho 2017), as it can be for targeted observations of stellar flares for individual stars (e.g. Mathioudakis et al. 2003). However, in order to identify more of these events for stellar flares, long-duration observations with a high cadence are required for a large number of stars. This became possible with the *Kepler* satellite, which was launched in 2009 and observed over 195 000 stars (Huber et al. 2014). Indeed, short-cadence observations from *Kepler* have been used to increase the number of white-light QPP detections (e.g. Balona et al. 2015; Pugh et al. 2016). However, only a small fraction of targets were observed in the 1-min short-cadence mode (e.g. Gilliland et al. 2010) and not for the full duration of the mission, reducing the potential for detecting QPPs with a short time-scale. Consequently, it is apparent that in order to increase not only the number of QPPs but also the high-energy flares observed, long-duration, wide-field observations are required with a high cadence for all stars.

This has become possible with NGTS, which is a ground-based transiting exoplanet survey and consists of 12 telescopes, each with a 520–890nm bandpass (Wheatley et al. 2018). Each camera operates with an exposure time of 10 s and has a field of view of $\approx$8 deg^2, resulting in a total instantaneous field of view of 96 deg^2. NGTS also benefits from high-precision autoguiding (McCormac et al. 2013), which, when combined with a pixel scale of 4.97 arcsec per camera, enables the use of centroid analysis to rule out false-positive planet candidates due to blended sources (Günther et al. 2017). With stable tracking and wide fields, NGTS is able to detect and resolve flares on both single and blended objects.

In this paper, we present the detection of a high-energy stellar flare with QPPs from the pre-main-sequence M star NGTS J121939.5–355557 (hereafter NGTS J1219–3555). This is one of the best resolved observations of stellar flare substructure from a wide-field survey, allowing us to apply methods developed for solar flares. We present our detection with NGTS and we discuss how we identified the source of the flare and derived its properties. We also present the oscillations of the flare and we assess their significance, along with comparing them to previous observations of stellar and solar QPPs.

2 OBSERVATIONS

The data presented in this paper were collected using NGTS over 115 nights between 2015 November 28 and 2016 August 4. The detected flare occurred on the night of 2016 January 31.

2.1 Flare detection

To identify flares in our data, we initially detrended the raw NGTS light curves using a custom version of the SYSREM algorithm. The full details of NGTS detrending pipeline can be found in Wheatley et al. (2018).

Stellar flares typically occur on time-scales of minutes to hours, meaning most flares will have a duration less than a single night.

We searched for flares on individual nights to make the most of this short time-scale.

When searching for flares within a single night, we employ a two-step flagging method. Initially, we search for regions in the night where at least three consecutive data points are six median absolute deviations (MADs) above the night median (as done by Jackman et al. 2018). For the majority of flares, due to the aforementioned time-scales, the median and MAD will not be strongly altered. Therefore, this method typically finds flares that occur purely within a single night. To find flares that dominate the entire night, we also check whether the median of a night is five MADs above the median of the entire light curve. This is indicative of a flare with a longer time-scale where we might only capture a portion of the event. After we have run this flagging procedure, we visually inspect all candidates to remove false positives. Examples of false positives include high-amplitude variable stars and satellites passing through our aperture.

Following this method, we detected a flare from the blended source NGTS J1219–3555. *Gaia* astrometry reveals that two sources reside within the NGTS aperture, separated by 6.7 arcsec. The flare, shown in Fig. 1, was flagged as the median of the night being five MADs above the median of the light curve. Fig. 1 shows the flare after we have removed the flux contribution from the background star, using the method described in Section 2.4. The two sources and the NGTS aperture are shown in Fig. 2.

Following the detection of the flare in Fig. 1, we checked each individual night to find low-amplitude flares that might not have been flagged. By doing this, we found three additional lower-amplitude flares towards the end of the season.

2.2 Centroid analysis

As two sources are present inside the NGTS aperture, we needed to determine on which star the flare occurred. To determine this, we use the centroid shift of the combined stellar image. For an isolated source, we expect the centre of our aperture $x_{\rm ap}(t)$ to be equal to the centre of flux $x_{\rm flux}(t)$. However, for a blended source, there is an offset from the primary source due to the secondary flux contribution. We can define the centroid $\xi(t)$ as the difference in position between the two, or

$$\xi(t) = x_{\rm flux}(t) - x_{\rm ap}(t). \quad (1)$$

During a flaring event, we would expect the centroid position to move towards the flaring source. This is similar to the use of centroiding to vet *Kepler* planet candidates (e.g. Bryson et al. 2013). A more detailed discussion of centroiding in NGTS and its use with blended sources can be found in Günther et al. (2017).

For this analysis, we utilized centroid positions calculated as part of the NGTS data analysis pipeline. Fig. 1 shows a comparison of the centroid position with time for the flare. We also compare this centroid movement with the images of the source before and during the flare, to confirm the position of the flaring source, identifying the source as NGTS J1219–3555. This is the south-east source in Fig. 2 and has previously been identified as 2MASS J12193970–3556017.

2.3 Stellar properties

2.3.1 Spectral energy distribution

With this positional information we obtained catalogue magnitudes, making sure to use only catalogues that are able to identify the two sources separately. The results of this matching are shown in

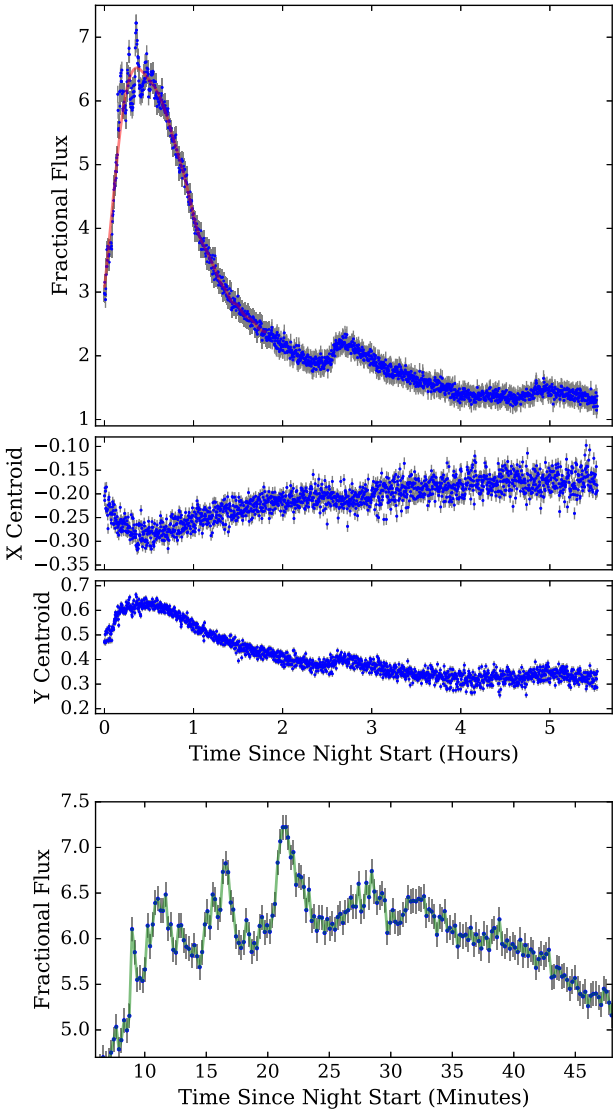

Figure 1. NGTS data from the night of the flare. Top: the flare after the removal of the background source flux, as discussed in Section 2.4. We do not show the quiescent nights before and after the flare, which are at an average value of 0 with this normalization. The trend of the flare from an EMD analysis is shown in red, as discussed in Section 3.4. Middle: centroid movement (in pixels) during the night, showing correlation with the flux. X and Y correspond to the movement along the axes specified in Fig. 2. Bottom: enlarged view of the flare's peak, in which oscillations are clearly seen. A flux spike, lasting only about 20–30 s, is seen at the beginning of the oscillations approximately 8 min after the start of the night. A green interpolating line is shown to aid the eye.

Table 2. Using the available information from the 2MASS (Skrutskie et al. 2006), *Gaia* (Prusti et al. 2016; Brown et al. 2018a), SkyMapper (Wolf et al. 2018) and the *Wide-field Infrared Survey Explorer* (*WISE*; Cutri et al. 2014), we performed spectral energy distribution (SED) fitting using PHOENIX models (Allard 2016). From this SED fitting and the *Gaia* Data Release 2 (DR2) parallax, we obtain estimates of stellar temperature and radius. We find an effective temperature of 3090 ± 30 K and a radius of $1.04 \pm 0.02\,{\rm R}_{\odot}$ for the flare star.

The large radius is not consistent with the expected value for a main-sequence M dwarf of this temperature ($\sim 0.2\,{\rm R}_{\odot}$; Mann et al. 2015), suggesting that NGTS J1219–3555 is not a single

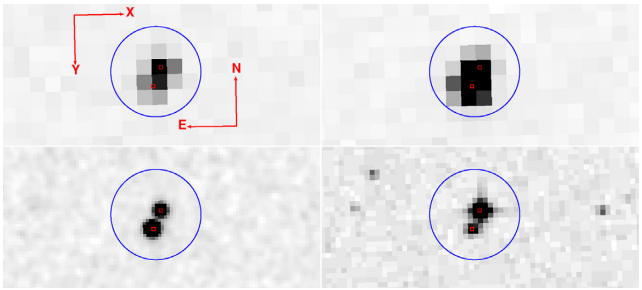

Figure 2. Comparison of NGTS images with Two-Micron All-Sky Survey (2MASS) and Sloan Digital Sky Survey (SDSS) images. The top-left panel is our reference image of the source, and the top-right is the image of the source at the peak of the flare. The flaring source is located at the south-east. The bottom-left panel is the available 2MASS image and the bottom-right panel is from the SDSS. The blue circle shows our aperture used, and red squares denote the positions of each individual source from *Gaia*. We have also plotted the NGTS image coordinate axes for reference with Fig. 1.

Table 1. Properties of the superflare detected from NGTS J1219–3555.

Property	Value
Energy (erg)	$>3.2 \pm^{0.4}_{0.3} \times 10^{36}$
Trend amplitude (per cent)	650
Peak flare amplitude (per cent)	720
Min duration (h)	5.5
Max duration (h)	42.4
e-folding duration (h)	1.8-2.6
Scale time (h)	1.3
QPP period, Fourier (s)	320^{+40}_{-35}
QPP period, EMD – modal (s)	316 (Mode 4), 682 (Mode 5)
QPP period, wavelet (s)	309 (Mode 4), 609 (Mode 5)
QPP amplitude (per cent)	10

main-sequence object. NGTS J1219–3555 is shown on a Hertzsprung–Russell (HR) diagram in Fig. 3, where it resides around 1.5 mag above stars of the same $G_{BP} - G_{RP}$ colour. If it were a binary star, we would expect it to reside no more than 0.753 mag above the main sequence (Babusiaux et al. 2018b), which is not consistent with our observation.

An alternative possibility is that NGTS J1219–3555 is a pre-main-sequence object. Interpolating the MESA Isochrones and Stellar Tracks (MIST) v1.1 models (Dotter 2016; Choi et al. 2016, with updated *Gaia* DR2 passbands and zero points) at the position of NGTS J1219–3555 in Fig. 3 and assuming zero interstellar reddening, we estimate an age of 2.2 Myr and a mass of 0.18 $M_\odot$. These correspond to a $T_{\rm eff}$ of 3180 K and a radius of 0.96 $R_\odot$, very similar to the values obtained from the SED fit above. We do not identify any infrared excess from our SED fitting on either star. This implies that if NGTS J1219–3555 is a pre-main-sequence star, then it has already lost the majority of any disc that was present during formation. Near- and mid-infrared disc fractions in young clusters and star-forming regions are consistent with median primordial disc lifetimes of 4–5 Myr for solar- and later-type stars (Bell et al. 2013; Pecaut & Mamajek 2016). This suggests that if NGTS J1219–3555 is as young as 2 Myr, then its disc dissipated earlier than expected, perhaps as a result of enhanced mass accretion because of strong flares (e.g. Orlando et al. 2011). We would expect a low-mass star such as NGTS J1219–3555 to be moving almost isothermally along its Hayashi track and thus it should remain at a similar $G_{BP} - G_{RP}$ colour as currently observed. As a further test, we compare the 2MASS *J*,*H*,*K* photometry of NGTS J1219–3555 with those from giants and dwarfs in Bessell & Brett (1988). By doing this, we find that NGTS J1219–3555 resides in the region occupied by dwarfs, supporting our interpretation that NGTS J1219–3555 is a pre-main-sequence star rather than a subgiant or an unresolved binary system.

From our SED fitting, we determine the neighbouring star to be a background G-type star. From the *Gaia* parallax and proper motions, it is clear that these two sources are unrelated, with the G-type star being much more distant than NGTS J1219–3555. The *Gaia* astrometry for NGTS J1219–3555 is not consistent with membership in any known young moving group, association or open cluster. Although spatially coincident with TW Hya Association members in the northern reaches of the Scorpius–Centaurus OB association, the 210 ± 3 pc distance to NGTS J1219–3555 means that it is likely to be a young background object or escapee from the region.

2.3.2 *Optical spectroscopy*

To confirm that NGTS J1219–3555 is a pre-main-sequence star, we acquired six 1800-s spectra on 2018 July 17 using the Wide-Field Spectrograph (WiFeS; Dopita et al. 2007) on the Australian National University (ANU) 2.3-m telescope at Siding Spring Observatory. The R7000 grating and RT480 dichroic used gave a resolution of $R \approx 7000$ over a wavelength range of 5250–7000 Å. Details of the instrumental set-up and reduction process are provided in Murphy & Lawson (2015). While the absence of strong emission lines other than Hα in the first spectrum indicates that the star was likely seen in quiescence, we appear to have serendipitously observed a flare event in subsequent spectra, with enhanced continuum emission, a rapid increase in the strength and width of the Hα and He I 5876/6678 Å emission lines and delayed Na D emission evident. These flare observations will be discussed further in a later work.

We observed NGTS J1219–3555 twice more in quiescence on July 18 and the average of the three quiescent spectra is plotted in Fig. 4. NGTS J1219–3555 is clearly of M spectral type, with strong Hα emission (EW $= -12 \pm 1$ Å) and Li I λ6708 absorption (EW $= 610 \pm 60$ mÅ). The uncertainty in each case is the standard deviation across the three observations. Comparing the spectra to M dwarf templates and radial velocity standards observed each night, we estimate a spectral type of M3–3.5 and we measure a mean radial velocity of 18.5 ± 1.4 km s^{-1}. Within the limits of the modest velocity resolution of WiFeS, the star's cross-correlation function is consistent with a slowly rotating ($v \sin i \lesssim 45$ km s^{-1}) single star (see the discussion in Murphy & Lawson 2015). We note that the SED and MIST $T_{\rm eff}$ values are 200–300 K cooler than the corresponding pre-main-sequence temperature (3360 K) for an M3 star from the scale of Pecaut & Mamajek (2013). However, their sample of mid-M pre-main-sequence stars was dominated by older, higher surface gravity stars from the 10–25 Myr old η Cha, TW Hya and β Pic moving groups, whereas NGTS J1219–3555 may be as young as 2 Myr.

The detection of essentially undepleted lithium in an M3 star is immediate evidence of youth. The MIST models above predict that a 0.18-$M_\odot$ star will retain its primordial lithium for 30–35 Myr, and then rapidly deplete the element to zero photospheric abundance by the age of 40 Myr. Therefore, any detection of lithium in such a star sets this as an upper age limit. By combining the lithium detection with the position of the star in Fig. 3, we are confident that NGTS J1219–3555 is a very young pre-main-sequence star.

Table 2. Parameters for our sources. References are: 1, *Gaia* (Brown et al. 2018a); 2, SkyMapper DR1.1 (Wolf et al. 2018); 3, 2MASS (Skrutskie et al. 2006); 4, *WISE* (Cutri et al. 2014). For distances, we have used the values from Bailer-Jones et al. (2018). SkyMapper magnitudes are AB magnitudes.

Parameter	Value (flaring)	Value (companion)	Reference
Position			
RA ICRS	184.°9153111262	184.°9144202	1
Dec. ICRS	–35.°9338316576	–35.°9321149	1
Photometric			
SkyMapper *u*	N/A	15.930 ± 0.009	2
SkyMapper *v*	N/A	15.523 ± 0.008	2
SkyMapper *g*	17.060 ± 0.009	14.521 ± 0.003	2
SkyMapper *r*	16.125 ± 0.011	14.227 ± 0.005	2
SkyMapper *i*	14.379 ± 0.014	14.063 ± 0.008	2
SkyMapper *z*	13.651 ± 0.004	14.019 ± 0.009	2
Gaia G	15.286 ± 0.001	14.237 ± 0.001	1
Gaia BP	16.972 ± 0.009	14.576 ± 0.001	1
Gaia RP	14.017 ± 0.003	13.738 ± 0.001	1
J	12.086 ± 0.024	13.162 ± 0.030	3
H	11.520 ± 0.025	12.846 ± 0.041	3
K_s	11.160 ± 0.021	12.842 ± 0.034	3
*W*1	11.000 ± 0.024	12.575 ± 0.049	4
*W*2	10.792 ± 0.021	12.594 ± 0.052	4
*W*3	10.778 ± 0.071	12.867 ± 0.463	4
*W*4	8.704	8.680	3
Kinematic			
μ_{RA} (mas yr^{-1})	–19.177 ± 0.108	–2.653 ± 0.108	1
μ_{Dec} (mas yr^{-1})	–8.490 ± 0.083	–4.644 ± 0.037	1
Parallax (mas)	4.733 ± 0.072	1.098 ± 0.032	1
Distance (pc)	210 ± 3	887 ± 26	
SED fit			
T_{eff} (K)	3090 ± 30	5610 ± 30	
R ($R_\odot$)	1.05 ± 0.02	1.22 ± 0.03	
X-ray emission			
L_X (erg s^{-1})	3×10^{29}		
$\log L_X/L_{Bol}$	−3.1		

2.3.3 *X-ray emission*

As a young and active pre-main-sequence star, we can expect NGTS J1219–3555 to be a relatively luminous X-ray source. Fortunately, it was observed serendipitously in X-rays with *XMM–Newton* for 27 ks on 2016 December 20 (ObsID, 0784370101; PI, Loiseau) and inspection of the pipeline-processed images shows that an X-ray source is indeed detected at the position of NGTS J1219–3555. The spatial resolution of the *XMM–Newton* telescopes is around 5 arcsec (Jansen et al. 2001) and the detected X-ray source is clearly centred on the position of the pre-main-sequence star, and not the background G star. There is no evidence for significant X-ray emission from this neighbouring object.

We extracted an X-ray light curve and spectrum for NGTS J1219–3555 from the EPIC-pn camera using the *Gaia* position and a 20-arcsec radius aperture. The background counts were estimated using a source-free circular region of radius 54 arcsec located nearby on the same CCD detector. We followed the standard data reduction methods as described in data analysis threads provided with the Science Analysis System[1] (SAS version 17.0). We found that a background flare had occurred during the final 4.2 ks of the *XMM–Newton* observation, and we excluded this interval when extracting the X-ray spectrum.

We inspected the X-ray light curve of NGTS J1219–3555 and found no evidence for significant variability during the *XMM–Newton* observation. This indicates that the observation was free of any large stellar flares and that the X-ray flux can be taken as representative of the quiescent level.

The X-ray spectrum of NGTS J1219–3555 is plotted in Fig. 5. We binned the spectrum to a minimum of 20 counts per bin, while ensuring that the spectral resolution would not be oversampled by more than a factor of 3, and we fitted the spectrum using XSPEC[2] (version 12.10).

The X-ray spectra of active late-type stars are characterized by optically thin thermal emission from the corona with temperatures typically in the range 10^6–10^7 K. We fitted the EPIC-pn spectrum of NGTS J1219–3555 using the APEC optically thin thermal plasma model (Smith et al. 2001). We found it necessary to include two APEC components (as an approximation to the expected multitemperature plasma) as well as photoelectric absorption by neutral material (using the TBABS model; Wilms, Allen & McCray 2000).

Initially, we set the elemental abundances to solar values (Asplund et al. 2009), but we found that the spectral fit was improved significantly around 1 keV by allowing the Fe and Mg abundances to drop below solar values (values of 0.03–0.19 solar). This is consistent with the inverse FIP effect seen in very active stars and M dwarfs (where FIP refers to the first ionization potential of the

[1] http://www.cosmos.esa.int/web/xmm-newton/sas

[2] https://heasarc.gsfc.nasa.gov/xanadu/xspec/

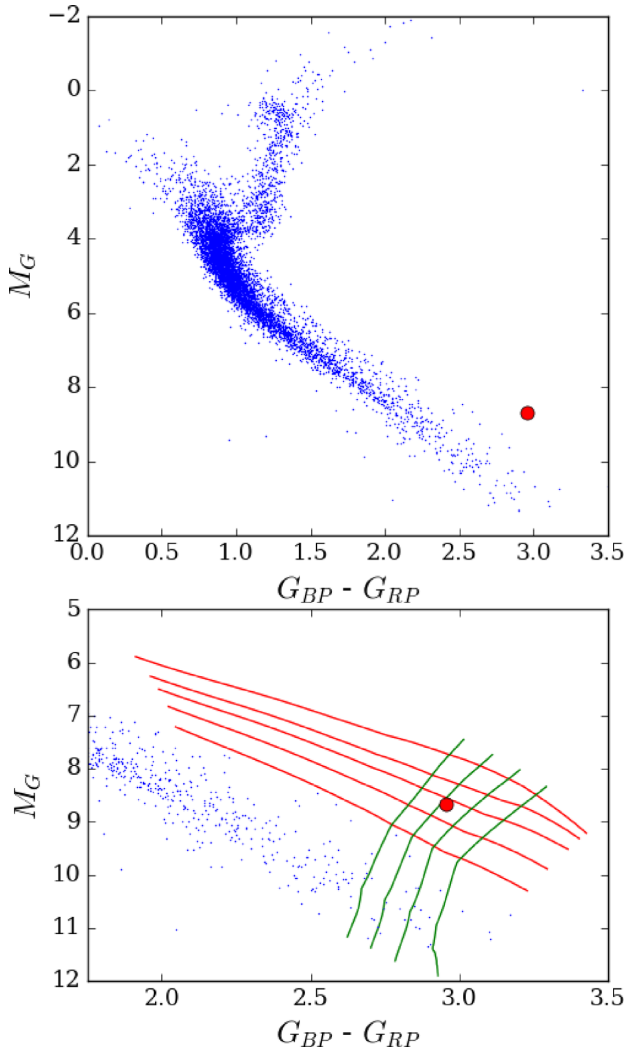

Figure 3. Top: HR diagram of *Gaia* crossmatched stars in our NGTS field. The red marker indicates the position of NGTS J1219–3555 approximately 1.5 mag above the main sequence. Bottom: the same HR diagram, but now zoomed in and with selected MIST models overlaid. Green lines (running top to bottom) indicate stellar mass tracks between 0.14 and 0.2 $M_\odot$ and red lines (running left to right) indicate isochrones of 1, 1.5, 2, 3 and 5 Myr.

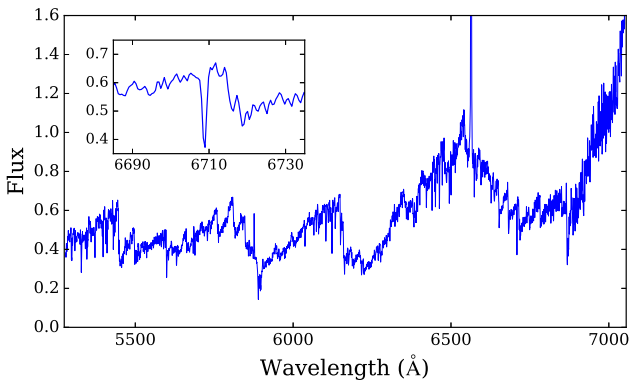

Figure 4. Mean quiescent WiFeS/R7000 spectrum of NGTS J1219–3555, normalized at 7000 Å. Hα continues to a peak flux of 6.5 on this scale. Inset is the Li I λ6708 absorption line.

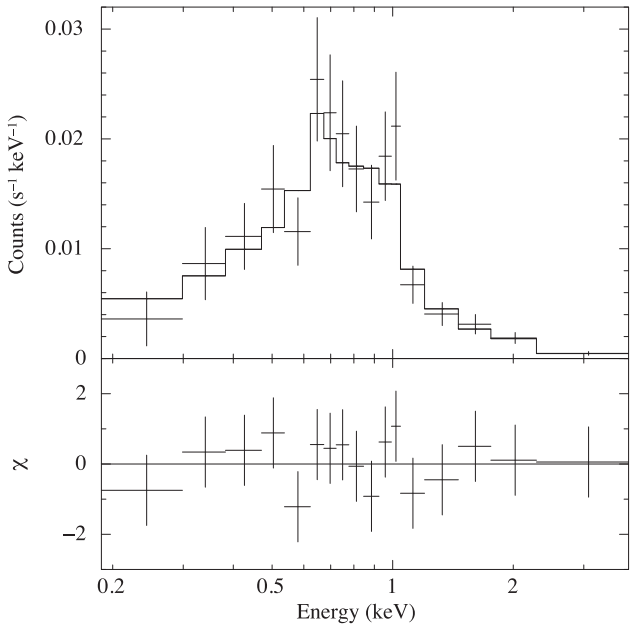

Figure 5. *XMM–Newton* EPIC-pn X-ray spectrum of NGTS J1219–3555 fitted using a two-temperature thermal plasma model, with abundances consistent with the inverse FIP effect, and circumstellar photoelectric absorption. The model and best fitting parameters are described in Section 2.3.3.

element; Wood & Linsky 2010; Wood, Laming & Karovska 2012; Laming 2015).

Our best-fitting model and residuals are also plotted in Fig. 5. The fitted absorption column density was found to be $N_{\rm H} = 1.2 \pm^{0.6}_{0.4} \times 10^{21}$ cm^{-2}, which is larger than the total Galactic column density in the direction of NGTS J1219–3555 ($N_{\rm H} = 0.65 \times 10^{21}$ cm^{-2}; Kalberla et al. 2005). This suggests that the line-of-sight absorption is dominated by circumstellar material, as might be expected for such a young star. The best-fitting temperatures in our model were $0.52 \pm^{0.08}_{0.12}$ and >2.5 keV (6 and >29 MK).

The absorbed X-ray flux in the energy range 0.1–2.5 keV is $3.3 \pm^{2.1}_{1.3} \times 10^{-14}$ erg s^{-1} cm^{-2}, corresponding to an X-ray luminosity of $1.6 \pm^{1.0}_{0.6} \times 10^{29}$ erg s^{-1} at a distance of 210 pc (Table 2). Setting the absorption column density in the model to zero, we can infer the inherent unabsorbed flux to be approximately 6×10^{-14} erg s^{-1} cm^{-2}, corresponding to an X-ray luminosity of 3×10^{29} erg s^{-1}. A comparison with the bolometric luminosity of the star (calculated from effective temperature and radius reported in Table 2) gives a ratio $\log L_{\rm X}/L_{\rm Bol} = -3.1$. This X-ray activity level is characteristic of saturated X-ray emission, as expected for a young and active star (e.g. de la Reza & Pinzón 2004; Stassun et al. 2004; López-Santiago et al. 2010).

2.4 Flux removal

To calculate the true flare amplitude and energy, we needed to remove the flux contribution from the background G star. To do this, we used the PHOENIX spectra from our SED fitting in Section 2.3.1 and the NGTS sensitivity curve from Wheatley et al. (2018) to estimate the NGTS count rates of the two sources. To account for sky extinction, we assumed an atmospheric transmission curve for an airmass of 1.5.

In this way, we found a predicted total flux within 7 per cent of the observed value and the expected ratio of flux from each source. We corrected the predicted total flux to match the observed value,

resulting in a quiescent NGTS count rate of 175 ± 20 ADU s^{-1} for the flaring star. We corrected the median level of our light curve to this value.

2.4.1 Stellar rotation

Once we had removed the background flux from the NGTS light curve, we investigated the possibility of light-curve modulation due to stellar rotation from NGTS J1219–3555. This was to identify potential starspots and active regions. To do this, we used a generalized Lomb–Scargle periodogram from the ASTROPY LombScargle package (Robitaille et al. 2013). The flares were removed from the light curve when calculating the periodogram. We sampled periods between 1 h and 25 d, requiring 10 samples per peak. This resulted in roughly 60 000 periods to sample on (VanderPlas 2018). The period of 25 d was chosen as our maximum period to avoid the lunar period. During our analysis, we masked suspicious periods due to 1 d aliases. We were unable to identify any convincing period of flux modulation from our analysis.

3 RESULTS

3.1 Flare amplitude and energy

To measure the maximum amplitude of the flare, we used the fractional flare amplitude, $\Delta F/F$, which gives the observed flare in units of the quiescent stellar flux. Using the value from Section 2.4 of 175 ± 20 ADU s^{-1} for the median flux level, we measured the maximum fractional flare amplitude as 7.2 ± 0.8. The quoted error here is larger than that shown in Fig. 1 because we have incorporated the error on the quiescent flux of both stars. In Fig. 1 and elsewhere, we use the NGTS errors for our analysis.

We calculate the flare energy following the method of Shibayama et al. (2013), assuming the flare emission to be from a blackbody of temperature of 9000 ± 500 K. Blackbody-like emission from flares has been observed previously on main-sequence M dwarfs (e.g. Hawley & Fisher 1992) and this method has been used for M dwarf flare calculations elsewhere (e.g. Yang et al. 2017). From this, we calculate the bolometric energy of the flare as $3.2 \pm^{0.4}_{0.3} \times 10^{36}$ erg. As we do not observe the entirety of the flare, this value acts as a lower limit. It is worth noting that this is roughly 10 000 times greater than the Carrington event energy of $\approx 10^{32}$ erg (Carrington 1859; Tsurutani et al. 2003).

We repeated our calculation for the three smaller flares that we have identified, and we obtain energies of $2.3 \pm 0.2 \times 10^{34}$, $7.2^{+0.7}_{-0.6} \times 10^{33}$ and $2.9 \pm 0.3 \times 10^{33}$ erg, respectively. Consequently, from a total of 484 h of observations of NGTS J1219–3555, we found four flares above 10^{33} erg in energy. This gives an estimated occurrence rate of flares above 10^{33} erg for NGTS J1219–3555 as 72 ± 36 flares per year.

3.2 Flare duration

To measure the flare duration, we make use of two time-scales to account for not observing the full extent of the flare. First, we use the e-folding time-scale, defined as the time from the flare maximum to 1/e of this value. We measure the e-folding time-scale initially as 1.8 h. However, at around 2.7 h in Fig. 1 there is a bump that increases the flux back above the 1/e threshold. It is uncertain whether this bump is due to this flaring event or from elsewhere on the flaring star, so we have decided to use our original e-folding time-scale of 1.8 h. From the centroid movement of this bump in Fig. 1, we are confident that this bump is not a result of the background star.

Secondly, we use the scale time, the duration for which the flare is above half the maximum flux value. This gives a measure of the flare rise without the uncertainties associated with determining where the flare begins. We calculate a scale time of 1.3 h. We can also put a limit on the minimum and maximum full duration of the flare, using nights before and after. We calculate the absolute minimum and maximum durations as 5.5 and 42.4 h, respectively.

3.3 Significance of the oscillations

In order to determine whether a statistically significant periodic component is present in the flare light curve, and if so to estimate its period, the Fourier power spectrum during the flare was examined, using the method from Pugh, Broomhall & Nakariakov (2017).

The finite nature of time-series data, combined with the trends and astrophysical noise seen in flares, means that the exact shape of the power spectrum will vary depending on where the start and end times of the flare light curve are defined. Therefore, the start and end times that gave the most visible periodic signal in the power spectrum were chosen manually. Flare power spectra tend to have a power that is related to the frequency by a power law, which might be due to trends and/or the presence of red noise, and this power-law dependence needs to be carefully accounted for when assessing the significance of a periodic signal. For this part of the analysis, the first step was to fit the power-law dependence with a simple model, which was done in log space where the power law appears as a straight line. A broken power-law model was used to account for white noise that starts to dominate at higher frequencies (Gruber et al. 2011), resulting in a levelling off of the power law. This model can be written as

$$\log\left[\hat{\mathcal{P}}(f)\right] = \begin{cases} -\alpha \log(f) + c & \text{if } f < f_{\text{break}} \\ -(\alpha - \beta)\log(f_{\text{break}}) - \beta \log(f) + c & \text{if } f > f_{\text{break}} \end{cases}, \quad (2)$$

where f_{break} is the frequency at which the power-law break occurs, α and β are power-law indices and c is a constant. We estimated the uncertainties of the fitted model by performing 10 000 Monte Carlo simulations using the uncertainties of the original light-curve data. The following initial parameters were used: $\alpha = 2.0$, $\beta = 0.1$, $c = -0.1$, $\log f_{\text{break}} = -1.8$. These were allowed to vary with a standard deviation equal to 10 per cent of the parameter values in order to reduce of the possibility of the least-squares fit finding a local minimum rather than the global minimum.

Two approaches were used to assess the significance of a peak in the power spectrum corresponding to a periodic signal. These approaches are based on the method described by Vaughan (2005) and account for data uncertainties as well as the power-law dependence of the spectrum. They make use of regular and binned power spectra and are explained in detail in Pugh et al. (2017).

From this analysis, we find a peak in the regular power spectrum corresponding to a period of 320^{+40}_{-35} s (or $5.2^{+0.7}_{-0.6}$ min), which reaches the 98.8 per cent confidence level, as shown by Fig. 6. The uncertainty was taken to be the standard deviation of a Gaussian model fitted to the peak. Because the peak in Fig. 6 appears to span more than one frequency bin, if we sum together the powers in every two frequency bins and assess the significance of the same peak in this binned power spectrum, shown by Fig. 7, then the peak reaches the 99.8 per cent confidence level. Hence, the periodic component

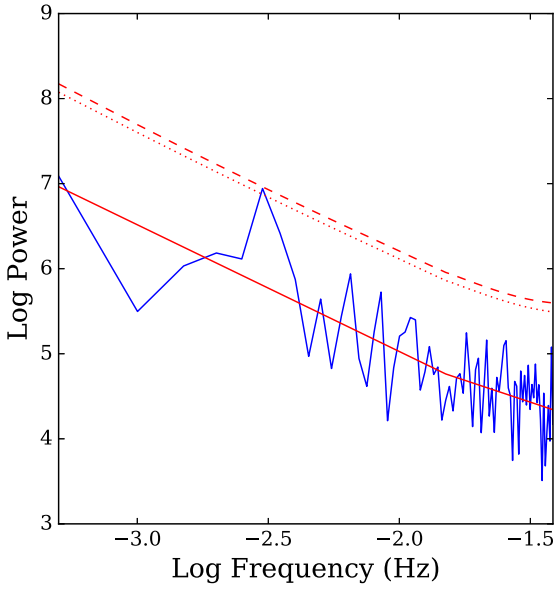

Figure 6. The regular power spectrum for the flare, shown in blue. The solid red line indicates the power-law fit, while the dotted and dashed lines are the 95 and 99 per cent confidence levels, respectively. This figure uses data between HJDs of 245 7419.6607291666 and 245 7419.6839814815.

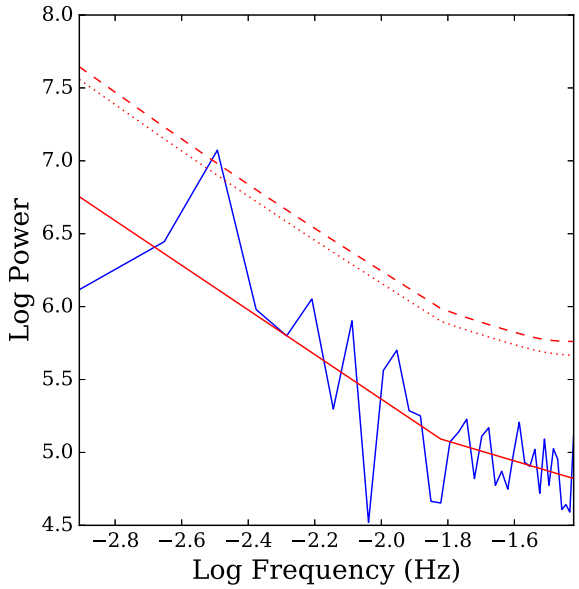

Figure 7. The binned power spectrum for the flare. This figure uses data between HJDs of 245 7419.6607291666 and 245 7419.684270833.

of the flare's light curve is highly significant and very unlikely to be the result of noise.

3.4 Empirical mode decomposition

An alternative method of investigating the periodicity of QPP signals is to use empirical mode decomposition (EMD; e.g. Kolotkov et al. 2015; Cho et al. 2016). This method has been utilized previously for solar and stellar QPPs and is used to reduce signals into intrinsic mode functions (IMFs), which can be used to describe natural time-scales appearing in the original data set. In particular, the combination of modes can be used to model the longer time-scale

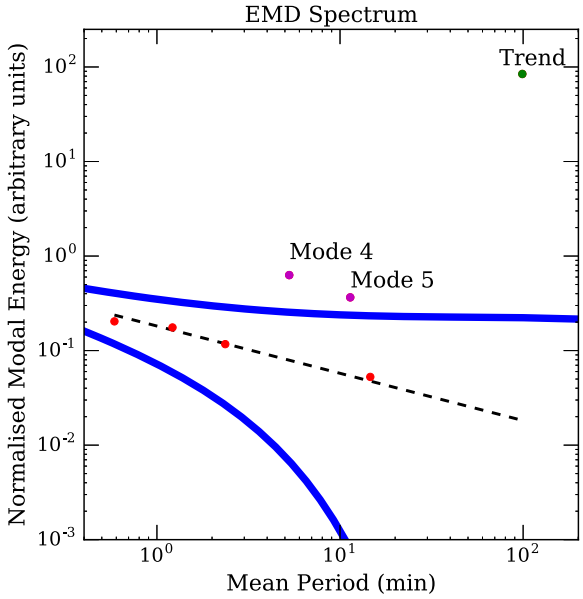

Figure 8. EMD spectrum for the identified modes, showing the normalized energy E_m versus the mean period P_m for each mode. Modes 4 and 5 are shown with magenta points, the trend is shown in green and all other modes are in red. The black dashed line is the expected behaviour ($E_m P_m^{1-\alpha} =$ const) for noise with $\alpha \approx 0.5$. Plotted in blue are the 99 per cent uncertainty levels, showing that modes 4 and 5 and the trend are statistically significant.

flare shape. We perform EMD on our flare and obtain seven modes, including the background trend. This trend contains the longest time-scale behaviour and is used to fit for the overall flare shape (see Fig. 1 for this trend on the flare peak), as it does not include substructure.

In order to determine whether these modes are statistically significant, we follow the method of Kolotkov, Anfinogentov & Nakariakov (2016), which we review briefly here. When performing EMD of coloured noise, the obtained IMFs have the relation $E_m P_m^{1-\alpha} =$ const, where E_m and P_m are the energy density and the modal period of each IMF and α is the power-law index. Note that α is used to describe the colour of the noise present, from the classical definition of the Fourier power spectral density S of the noise, $S = C/f^{\alpha}$. For example, $\alpha = 0$ for white noise, 1 for pink noise and 2 for red noise. Using this IMF energy–period relation and assuming that all modes follow the same noise power, by plotting the energy and period of each mode in logarithmic space and using a linear fit,we should find α. However, any modes with different behaviour, because of some underlying process, will lie off this line. We perform this for our modes, giving $\alpha \approx 0.5$, shown in Fig. 8, which suggests low levels of correlated noise. We can see in Fig. 8 that modes 4 and 5 and the background trend lie off this fitted model, suggesting that additional signals are present in these modes that cannot be explained by noise. Using the full method from Kolotkov et al. (2016), we calculate 99 per cent significance levels for $\alpha = 0.5$ noise, shown by the blue lines in Fig. 8 for the upper and lower confidence levels. As a result, we see that modes 4 and 5 are statistically significant and we proceed to analyse their morphology, regarding the other modes as noise. The trend is also outside this confidence interval, as expected.

For part of the above method, we calculated the average modal periods of modes 4 and 5. These are 316 and 682 s, respectively. As another test, we also follow the method of Kolotkov et al. (2015) and use a Hilbert transform to calculate their instantaneous

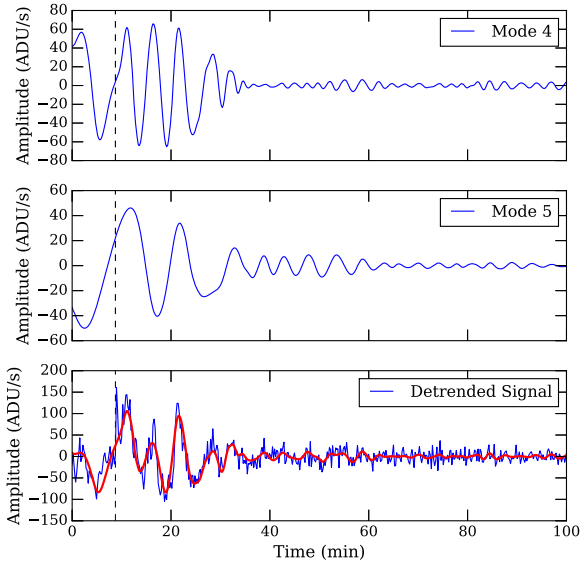

Figure 9. Modes 4 and 5 from the EMD analysis. The bottom panel shows these combined (red) over the trend-subtracted flare peak. The dashed vertical line indicates the start of a flux pulse, as discussed in Section 4.

frequencies and periods. Constraining our region to the same area used in Section 3.3, we obtain median instantaneous periods of 338 and 625 s for modes 4 and 5, respectively. To obtain an estimate of the period error, we use the mean and the standard deviation of these periods, giving periods of 327 ± 11 and 654 ± 30 s for modes 4 and 5 respectively.

3.4.1 QPP signal and amplitude

Fig. 9 shows modes 4 and 5, along with their combination and the trend-subtracted flare. We can see that the combination of both modes is able to reproduce the observed QPPs. We note that the periodicity of mode 4 appears to begin after a 20-s duration spike in flux, approximately 8 min into the night, whereas mode 5 is present from the start of the night. This spike in flux is also clearly visible in Fig. 1. We can use the trend in conjunction with the QPP signal also to determine the fractional flux amplitude, $\Delta F_{\rm osc}/F_{\rm tr}$, of the oscillations, where $F_{\rm tr}$ denotes the trend flux. By doing this and ignoring the flux spike, we obtain the fractional flux of the combined oscillations $\Delta F_{\rm osc}/F_{\rm tr} = 0.1$.

3.4.2 Wavelet analysis

In order to help confirm the periodicities from our previous two methods, we have performed a wavelet analysis. This was done by incorporating the method of Auchère et al. (2016), which takes into account the total number of degrees of freedom of the wavelet spectrum when assessing the significance of identified peaks in power. To perform this analysis, we used a detrended light curve, obtained by dividing our light curve by the overall flare trend identified through our EMD analysis. The results of our wavelet analysis are shown in Fig. 10 where we can see two peaks in power, at 309 and 609 s. These agree with the period identified from our power spectrum analysis and the two periods identified with the EMD analysis, adding weight to the fact that there are two periods present. The ratio between these periods suggests that they might be harmonics of the same MHD mode, something which we discuss in Section 4.5.

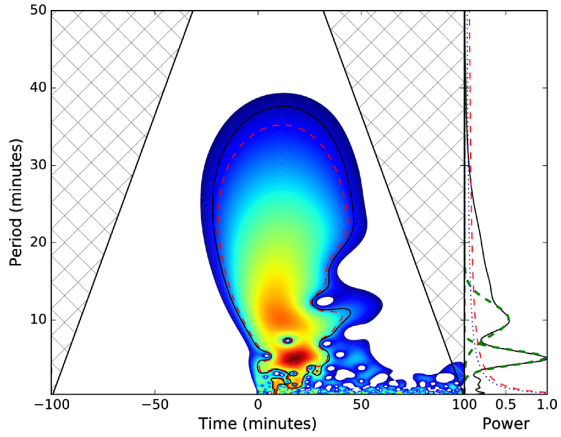

Figure 10. Wavelet analysis of the flare, showing two peaks at 309.2 and 608.5 s, respectively. Red depicts the periods with greatest power. The black wavelet boundary is the 99 per cent confidence level and the red line is the modified confidence level, based on Auchère et al. (2016). The panel on the right of the figure shows the peaks of the two components, with Gaussian fits in green.

The 309-s period appears to show a slight offset from the 609-s peak, something that is also seen in our EMD analysis and is also discussed in more depth in Section 4.5.

4 DISCUSSION

We have detected a large white-light stellar flare from the pre-main-sequence M star NGTS J1219–3555. This star is extremely young with an estimated age of 2.2 Myr and undepleted lithium in the stellar spectrum. From SED fitting and optical spectroscopy, we estimate a spectral type of M3–3.5. The flare displays multi-mode QPPs in the peak. We have calculated the energy of this flare as $3.2 \pm^{0.4}_{0.3} \times 10^{36}$ erg and the maximum amplitude as 7.2 ± 0.8. Using multiple methods, we have identified the periods of oscillations as approximately 320 and 660 s, with an oscillation amplitude $\Delta F_{\rm osc}/F_{\rm tr}$ of 0.1. The 320-s oscillation mode appears to begin after a 20–30 s spike in flux during the rise of the flare. The observation of this spike and the resolution at which the 320-s mode is seen is a testament to the high cadence of NGTS compared to the *Kepler* and *TESS* short-cadence modes, which would not obtain such detail.

4.1 Flare energy

In Section 3.1, we calculated the lower limit of the flare energy as $3.2 \pm^{0.4}_{0.3} \times 10^{36}$ erg. This energy is greater than all M dwarf flares observed with *Kepler* by Yang et al. (2017) and it is comparable to that emitted by the highest energy G star superflares (e.g. Shibayama et al. 2013; Wu, Ip & Huang 2015). This value sits within the range of bolometric flare energies calculated for 3-Myr stars in NGC 2264 by Flaccomio et al. (2018), using targeted *CoRoT* observations. It is also similar to the energies of flares observed from long-cadence K2 observations of the 1-Myr brown dwarf CFHT-BD-Tau 4 by Paudel et al. (2018).

As mentioned in Section 3.1, because we have not observed the entirety of the flare, this energy is a lower limit. Previous works that have observed only a portion of long-duration flare events have been able to estimate the full energy by using empirical flare models to obtain the full shape of the flare (Schmidt et al. 2016). These models typically assume that the flare is a simple event (i.e. with

no significant substructure; e.g. Davenport et al. 2014; Jackman et al. 2018). However, complex flares such as the flare we have observed do not strictly follow such models and have a range of morphologies (e.g. multiple peaks). Consequently, we have decided against applying an empirical flare model to estimate the full energy.

When calculating the bolometric energy, it was assumed that the flare could be modelled as a 9000-K blackbody. This method assumes that the spectrum of the flare is constant for the total duration. Previous observations have shown that this might not be the case (e.g. Kowalski et al. 2013) and this has resulted in other works resorting to alternative methods. One commonly used method is to calculate the equivalent duration of the flare and to multiply this by the quiescent luminosity of the star in the instrument bandpass (e.g. Hawley et al. 2014; Davenport 2016; Vida et al. 2017). For our observed flare, we have decided not to use such a method. Our reasoning for this is that using the quiescent luminosity in such a way assumes that the flare emits with the same spectrum as the star, which for M stars is not the case – particularly over a wide bandpass such as NGTS. By using a 9000-K blackbody, we expect to remain close to an expected flare spectrum.

4.2 Occurrence rate of flares

In Section 3.1 we estimated the occurrence rate for flares above 10^{33} erg as 72 ± 36 per yr for NGTS J1219–3555. For the flare in Fig. 1, a simple scaling of a single detection in 484 h gives an estimated occurrence rate for flares above 10^{36} erg for NGTS J1219–3555 alone as 18 per yr. A more reliable estimate can be made by assuming that stellar flares on NGTS J1219–3555 occur with a power-law distribution of flare energies (e.g. Lacy, Moffett & Evans 1976). By normalizing to our lower energy occurrence rate, we can estimate the distribution at higher energies.

From X-ray observations of the Orion Nebula Cluster by Caramazza et al. (2007), the power-law index of the X-ray flares of low-mass stars has been measured as 2.2 ± 0.2. However, from simultaneous optical and X-ray observations, Flaccomio et al. (2018) have shown that X-ray flares do not always have an optical counterpart. From their analysis, between 19 and 31 per cent of X-ray flares lack an optical counterpart. Consequently, as our observation is of a white-light flare, we have decided to make use of power-law indices obtained from white-light measurements. The power-law index for white-light flares on active M stars has been measured for both individual stars (e.g. Moffett 1974; Lacy et al. 1976; Ramsay & Doyle 2015) and groups (e.g. Hilton 2011). These measurements have shown that active M stars can have a range of power-law indices. Because of this scatter, we have chosen a range of power-law indices for predicting the flare rate. We have chosen limits of 1.53 and 2.01, taken from Hawley et al. (2014) and Hilton (2011) for observations of active M stars. We note that the upper limit here is still similar to that from Caramazza et al. (2007). With these values for the power-law index and our lower energy occurrence rate, we re-estimate our occurrence rates for flares above 10^{36} erg from NGTS J1219–3555 as between 3 ± 1.5 per yr and 2 ± 1 per decade.

While this is a wide range of values, it provides a more robust estimate of the occurrence rate of high-energy flares from NGTS J1219–3555. However, it has previously been noted that the occurrence rate drops off at the highest energies, giving a broken power law (e.g. Davenport 2016). As this break energy can vary from star to star, we have not incorporated this into our estimations. However, we do note that if our flare is in the 'drop off' regime then this would make it even rarer than our estimations above. This highlights not only the rarity of this event, but also the need for long-duration wide-field surveys such as NGTS to find them.

4.3 Flare amplitude

We can compare this flare to previous white-light observations of QPP-bearing stellar flares and we can see that it is the largest observed for its period time-scale (between 5 and 15 min) and one of the largest detected overall. The maximum change in NGTS magnitude is $\Delta m_{\rm NGTS} = 2.28$ for $\Delta F/F = 7.2 \pm 0.8$. The flares from II Peg and EV Lac, observed by Mathioudakis et al. (2003) and Zhilyaev et al. (2000), respectively, had a similar oscillation period. These both had observations in the *U* band, with flare amplitudes of 0.85 and ≈ 2.5. As stellar flares are blue in colour (particularly during the impulsive phase), we would expect increased amplitudes in the *U* band compared to the NGTS bandpass (e.g. as for *Kepler*; Hawley et al. 2014). Using our SED fit from Section 2.3.1 with the assumed 9000-K flare blackbody (using a Sloan SDSS *U*-band filter[3]) we estimate $\Delta m_U = 6$ for the observed flare, equivalent in amplitude to the 32-min period oscillating megaflare on YZ CMi (Kowalski et al. 2010; Anfinogentov et al. 2013). Consequently, we believe that this flare is one of the largest observed in white light, showing QPPs for both its period time-scale and possibly overall.

4.4 Formation and habitability of M star exoplanet systems

Flares and associated coronal mass ejections (CMEs) from pre-main-sequence stars could have an important role in planetary formation and habitability. For example, these transient events have been proposed as a possible mechanism for the formation of chondrules found in meteorites (Feigelson 2010). The flash-melting of these rocks requires a transient heat source, which could be provided either by direct absorption of flare XUV irradiation (Shu et al. 2001), or through a flare-associated shock wave (Nakamoto et al. 2005).

Flares and CMEs have also been linked to high stellar mass-loss rates by Osten & Wolk (2015) for young stars. For those with debris discs, CMEs have been highlighted as a possible cause of observed infrared variability. This is because of the removal of infrared-emitting dust by CMEs on the time-scales of days (Osten et al. 2013). For protoplanetary discs, large X-ray flares could, along with altering the structure and ionization fraction of the disc (e.g. Ilgner & Nelson 2006), cause increased mass transfer from the disc on to the star. This is through perturbations from flare loops linking the star and inner disc (Orlando et al. 2011), which result in bursts of accretion.

Once planets are formed, they will also be subject to irradiation from flares and CMEs. The transient increase of the stellar wind through CMEs can negatively influence the formation of a planetary dynamo (Heyner, Glassmeier & Schmitt 2012), resulting in a weakened planetary magnetic field. The planetary magnetic field is one of the main defences against the detrimental effects of CMEs, which can compress the planetary magnetosphere and expose the atmosphere to erosion (e.g. Kay, Opher & Kornbleuth 2016). Along with this, X-ray and UV irradiation from the flare itself might cause intense planetary ozone depletion (Segura et al. 2010), altered atmospheric chemical abundances (Venot et al. 2016) and potential

[3] http://svo2.cab.inta-csic.es/svo/theory/fps3/index.php?id=SLOAN/SDSS.u&&mode=browse&gname=SLOAN&gname2 = SDSS#filter

damage to the DNA of surface organisms (e.g. Lingam & Loeb 2017).

M stars have been noted for emitting less steady-state NUV radiation compared to earlier spectral types. This could limit possible UV-sensitive prebiotic chemistry (e.g. Ranjan et al. 2017), calling into question whether or not life could appear in these systems. The highest-energy flares such as the one observed have been suggested as a possible way of delivering required levels of UV irradiation to kick-start such prebiotic reactions (Buccino, Lemarchand & Mauas 2007; Ranjan et al. 2017; Rimmer et al. 2018). Because of the rarity of these high-energy events, studies of their occurrence rates (as in Section 4.2) with surveys such as NGTS are vital in helping to determine whether prebiotic chemistry could take place or whether more negative effects limit habitability.

4.5 MHD modes

Using modes 4 and 5 generated from the EMD method outlined in Section 3.4, we found that the QPPs could be reproduced. We calculated the average modal periods as 316 and 682 s, and their median instantaneous periods as 338 and 625 s, respectively.

These instantaneous periods were obtained by using the region of data used in Fig. 6, from the flare peak. We note that this still includes a small section in the flare tail where the oscillations are indistinguishable from the noise in the data. Excluding this and constraining the Hilbert spectrum region further results in instantaneous periods of 330 and 660 s for modes 4 and 5, respectively. The period for mode 4 is in agreement with the period obtained from Section 3.3 and this brings the period of mode 5 into better agreement with its average modal period. Therefore, the period ratio for modes 4 and 5 is approximately 2, as would be expected if these modes were fundamental and secondary harmonics. However, we note that even for harmonics this period ratio can deviate from 2 due to the dispersive nature of some MHD waves and the local geometry (e.g. Inglis & Nakariakov 2009).

We note also that the appearance of modes 4 and 5 is similar to that of modes 4 and 5 from Kolotkov et al. (2015), which had oscillation periods of 45 and 100 s and were thought to be potentially harmonics of the MHD kink mode. The period ratio of modes 4 and 5 suggests that they are both from the same MHD process, possibly a standing slow magneto-acoustic wave. In this mode, excitations of both the fundamental and second harmonic can be produced, with their relative amplitudes being dependent on the location of the flare trigger. Specifically, pulses closer to the flare loop footpoint will excite the fundamental mode, whereas those closer to the apex will excite the second harmonic (Selwa, Murawski & Solanki 2005). Selwa et al. (2005) also found that pulse triggers in locations other than the apex and footpoint can result in the excitation of a packet of standing waves with different modes, with the lowest-frequency two modes having the greatest contribution.

If this were the case, we would expect mode 4 to have an appearance similar to mode 5 (i.e. that of an exponentially decaying sinusoid). However, the appearance of mode 4 is more similar to that of previously observed wave trains (e.g. Nakariakov et al. 2004), which occur as a result of fast magneto-acoustic waves propagating in the plasma non-uniformity. These wave trains are highly dispersive in nature and can be created via an impulsive driving pulse or perturbation (Roberts, Edwin & Benz 1984). We observe a spike in flux during the rise of the flare, after which the observed periodicity of mode 4 begins immediately. This flux spike lasts for approximately 20–30 s in total, meaning it would not be identified in *Kepler* or *TESS* short-cadence observations. The amplitude of this spike is greater than the detrended signal, making it possible that this is a driving pulse that triggers the appearance of mode 4. A similar example has been observed in the Sun by Nisticò, Pascoe & Nakariakov (2014), where a pulse from a single source set off a quasi-periodic wave train. We do not see a similar change in period from mode 5 in Fig. 9.

This behaviour is also seen in Fig. 10 from our wavelet analysis, where the shorter-period peak is offset from the longer period. Consequently, we propose that this is a broad-band driving pulse, which results in the excitation of a quasi-periodic wave train (Nakariakov & Melnikov 2009b; Nakariakov et al. 2016), resulting in mode 4. This wave train could then be a combination of fast magneto-acoustic harmonics.

4.5.1 Mode 5

As mentioned previously, mode 5 does not share a similar appearance to mode 4 and seems generally unaffected by the observed flux spike. Instead, it has the appearance of a decaying mode with a damping time of ∼20 min. Comparing this damping time with the oscillation period of ∼660 s, we find it is in agreement with the upper limit of the relation found by Ofman & Wang (2002). This relation is for the oscillation period and damping time-scale of hot flare loops observed by the SUMER instrument onboard the *Solar and Heliospheric Observatory* (*SOHO*; Wang 2011).

To test the hypothesis that mode 5 is indeed the result of a standing slow mode, we can compare the period ratio between our two modes. If we assume that the coronal loop is represented by a magnetic cylinder of radius a and length L, in the low β limit (where magnetic pressure dominates), then we can write the period of mode 4 as

$$P_1 = \frac{2\pi a}{j_{0,1} v_\mathrm{A}} \left(1 - \frac{\rho_\mathrm{e}}{\rho_\mathrm{o}}\right), \tag{3}$$

where v_A is the Alfvén speed within the loop, ρ_e and ρ_o are the external and internal plasma densities and $j_{0,1}$ is the first zero of the Bessel function $J_0(z)$ (Roberts et al. 1984). For $\rho_\mathrm{e} \ll \rho_\mathrm{o}$, the fast mode is highly dispersive. Consequently, the bracketed term reduces to unity and we can rewrite equation (3) as

$$P_1 \approx \frac{2.62a}{v_\mathrm{A}}. \tag{4}$$

For a standing slow mode, the period, P_2, is given by Roberts et al. (1984) as

$$P_2 \approx \frac{2L}{c_\mathrm{s}}, \tag{5}$$

where c_s is the internal sound speed of the cylinder. From our observations, $P_2/P_1 \approx 2$, so

$$\frac{P_2}{P_1} = \frac{2L}{c_\mathrm{s}} \frac{v_\mathrm{A}}{2.62a}, \tag{6}$$

which approximates to $(v_\mathrm{A} L)/(c_\mathrm{s} a)$. Hence, $L/a \approx 2(c_\mathrm{s}/v_\mathrm{A})$. The Alfvén speed is typically greater than the sound speed, resulting in $L < a$ (i.e. the length of the cylinder is less than its radius). This is an unrealistic expectation for coronal loops and is not supported by observations from solar flares, making it unlikely that mode 5 is a standing slow mode. An alternative option is that mode 5 is instead a standing kink mode with a decaying amplitude. The period of a standing kink mode is given by Edwin & Roberts (1983) as

$$P_2 \approx \frac{2L}{c_\mathrm{k}}, \tag{7}$$

where c_k is the internal kink speed and, in this low β regime, it is approximately $\sqrt{2}v_A$ (e.g. Nakariakov & Ofman 2001). From this, we can write the period ratio P_2/P_1 as

$$\frac{P_2}{P_1} = \frac{2L}{c_k}\frac{v_A}{2.62a}. \quad (8)$$

This approximates to $L/2a = 2$, or $L/a = 4$, which is closer to what we would expect from a coronal cylinder (e.g. Van Doorsselaere et al. 2011). Standing kink oscillations associated with flaring events have been observed previously on the Sun (e.g. Ofman & Wang 2008; Zimovets & Nakariakov 2015; Goddard et al. 2016) and have previously been suggested as the cause of QPPs in some observed stellar flares (e.g. Anfinogentov et al. 2013). Consequently, we propose that a plausible explanation for mode 5 is a standing kink mode that was triggered at the start of the flare.

4.6 Seismology of mode 4

The generation of impulsive fast waves can be used to investigate the behaviour of the oscillating region. To do this, we rearrange equation (4), to obtain the ratio between a and v_A. We can then substitute in our observed fast mode period of 320 s to determine the ratio as $a/v_A = 123$ s.

If we assume the cylinder radius of 1×10^{10} cm, similar to X-ray flares previously observed on pre-main-sequence stars (e.g. Favata et al. 2005; López-Santiago et al. 2010), we estimate the Alfvén speed as 8×10^7cm s^{-1}. This estimated value is similar to the values calculated for QPPs from main-sequence M4 stars (e.g. Zaitsev et al. 2004; Mitra-Kraev et al. 2005; Anfinogentov et al. 2013), suggesting that our assumed cylinder radius value is a sensible one. Following this, if we use an aspect ratio of $\simeq 0.25$ (e.g. Mathioudakis et al. 2003), then the loop length is $\simeq 0.55R_*$. Assuming the loop is semicircular, we also estimate the height as $\simeq 0.18R_*$, similar to the average loop height for X-ray detected flares from pre-main-sequence stars studied by Flaccomio et al. (2018).

This ratio of loop length to stellar radius, while too large for the Sun and similar spectral types, is consistent with previous inferred measurements of loop lengths on main-sequence M dwarfs (which can be up to $2R_*$ in length; Mullan et al. 2006) and is well within loop lengths for pre-main-sequence stars (e.g. Favata et al. 2005; Johnstone et al. 2012). Indeed, for stars with a measured near-infrared excess, Favata et al. (2005) measured loop lengths up to tens of times the stellar radii, with the flaring loops connecting the star and disc. For stars in their sample with no measurable near-infrared excess (such as we find for NGTS J1219–3555), Favata et al. (2005) found more compact loop lengths, similar to what we find for NGTS J1219–3555. These smaller loops were suggested to be anchored into the photosphere only.

4.7 Flare decay

We also note the flare exhibits a bump at about 2.6 h after the start of the night and another at 4.9 h. Relative to the flare peak, these are 2.3 and 4.6 h afterwards. Bumps have been observed in *Kepler* stellar flares by Balona et al. (2015) who argued that they cannot be due to simultaneous independent flaring events, nor due to forced global oscillations. One possibility is that while these bumps are not from independent flares, they are instead due to sympathetic flaring. Sympathetic flaring occurs when the primary flare triggers a successive flare, due to a physical connection (Moon et al. 2002). Such behaviour would result in the observed flux increases in the flare tail, making it a possible cause.

5 CONCLUSIONS

In this work, we have detected a high-energy stellar flare from the 2-Myr-old pre-main-sequence M star NGTS J1219–3555 with NGTS. This flare has a minimum energy of $3.2 \pm^{0.4}_{0.3} \times 10^{36}$ erg, making it one of the largest energy M star flares observed. In the peak of this high-energy flare, we have detected statistically significant QPPs with an oscillation amplitude $\Delta F_{osc}/F_{tr}$ of 0.1. We have applied techniques typically used for analysis of solar flare QPPs to determine that the pulsations were formed of two distinct modes. The periods of these modes are approximately 320 and 660 s. With a measured amplitude of $\Delta m_{NGTS} = 2.28$ and an estimated amplitude of $\Delta m_U = 6$, we believe this is one of the largest white-light stellar flares to show QPPs of this time-scale, if not QPPs in general.

Investigating these modes further, we have identified that the shorter-period mode appeared after a high-amplitude spike in flux during the flare rise. This spike lasted for 30 s and was only resolvable due to the high cadence of the NGTS. We postulate that the short-period mode is a highly dispersive fast mode excited by the observed flux spike, similar to events seen in the Sun. We hypothesize that the longer-period mode is a kink mode excited at the flare start, although we cannot categorically rule out other proposed methods for the QPP excitation (McLaughlin et al. 2018).

We have also detected three more lower-energy flares in our data. Using these to estimate the flare occurrence rate, we find the high-energy flare to be a rare event, with a possible occurrence rate of between 3 ± 1.5 per year and 2 ± 1 per decade, depending on the power-law index of the assumed flare distribution. We use this to stress the importance of wide-field, long time-scale surveys such as the NGTS in finding these high-energy events, which must also have high cadence in order to characterize oscillation modes. Not only does this constrain their occurrence rates, but it also helps to determine their role in the formation and habitability of Earth-like exoplanets around M-type stars.

ACKNOWLEDGEMENTS

This research is based on data collected under the NGTS project at the ESO La Silla Paranal Observatory. The NGTS facility is funded by a consortium of institutes consisting of the University of Warwick, the University of Leicester, Queen's University Belfast, the University of Geneva, the Deutsches Zentrum für Luft- und Raumfahrt e.V. (DLR; under the 'Großinvestition GI-NGTS'), the University of Cambridge, together with the UK Science and Technology Facilities Council (STFC; project reference ST/M001962/1). JAGJ is supported by STFC PhD studentship 1763096. PJW and RGW are supported by the STFC consolidated grant ST/P000495/1. AMB acknowledges the support of the Institute of Advanced Study, University of Warwick, and is also supported by the STFC consolidated grant ST/P000320/1. MNG is supported by the STFC award reference 1490409 as well as the Isaac Newton Studentship. CEP acknowledges support from the European Research Council under the SeismoSun Research Project No. 321141. JSJ acknowledges support by Fondecyt grant 1161218 and partial support by CATA-Basal (PB06, CONICYT). DYK acknowledges support by the STFC consolidated grant ST/P000320/1. GMK is supported by the Royal Society as a Royal Society University Research Fellow. We also acknowledge and thank the ISSI team led by AMB for useful discussions.

This publication makes use of data products from the 2MASS, which is a joint project of the University of Massachusetts and the Infrared Processing and Analysis Center/California Institute

of Technology, funded by the National Aeronautics and Space Administration and the National Science Foundation. This publication makes use of data products from the *WISE*, which is a joint project of the University of California, Los Angeles, and the Jet Propulsion Laboratory/California Institute of Technology, funded by the National Aeronautics and Space Administration. The national facility capability for SkyMapper has been funded through ARC LIEF grant LE130100104 from the Australian Research Council, awarded to the University of Sydney, the Australian National University, Swinburne University of Technology, the University of Queensland, the University of Western Australia, the University of Melbourne, Curtin University of Technology, Monash University and the Australian Astronomical Observatory. SkyMapper is owned and operated by the Australian National University's Research School of Astronomy and Astrophysics. The survey data were processed and provided by the SkyMapper Team at the ANU. The SkyMapper node of the All-Sky Virtual Observatory (ASVO) is hosted at the National Computational Infrastructure (NCI). Development and support the SkyMapper node of the ASVO has been funded in part by Astronomy Australia Limited (AAL) and the Australian Government through the Commonwealth's Education Investment Fund (EIF) and National Collaborative Research Infrastructure Strategy (NCRIS), particularly the National eResearch Collaboration Tools and Resources (NeCTAR) and the Australian National Data Service Projects (ANDS). This work has made use of data from the European Space Agency (ESA) mission *Gaia* (https://www.cosmos.esa.int/gaia), processed by the *Gaia* Data Processing and Analysis Consortium (DPAC; https://www.cosmos.esa.int/web/gaia/dpac/consortium). Funding for the DPAC has been provided by national institutions, in particular the institutions participating in the *Gaia* Multilateral Agreement.

REFERENCES

Allard F., 2016, in Reylé C., Richard J., Cambrésy L., Deleuil M., Pécontal E., Tresse L., Vauglin I., eds, SF2A-2016: Proceedings of the Annual meeting of the French Society of Astronomy and Astrophysics, Société astronomique de France, Paris, p. 223
Anfinogentov S., Nakariakov V. M., Mathioudakis M., Van Doorsselaere T., Kowalski A. F., 2013, ApJ, 773, 156
Asplund M., Grevesse N., Sauval A. J., Scott P., 2009, ARA&A, 47, 481
Auchère F., Froment C., Bocchialini K., Buchlin E., Solomon J., 2016, ApJ, 825, 110
Babusiaux C. et al., 2018b, A&A, 616, 10
Bailer-Jones C. A. L., Rybizki J., Fouesneau M., Mantelet G., Andrae R., 2018, AJ, 156, 58
Balona L. A., Broomhall A.-M., Kosovichev A., Nakariakov V. M., Pugh C. E., Van Doorsselaere T., 2015, MNRAS, 450, 956
Bell C. P. M., Naylor T., Mayne N. J., Jeffries R. D., Littlefair S. P., 2013, MNRAS, 434, 806
Berger E., Fong W., Sanders N., Chornock R., 2012, The Astronomer's Telegram, 4619
Berger E. et al., 2013, ApJ, 779, 18
Bessell M. S., Brett J. M., 1988, PASP, 100, 1134
Brown A. G. A. et al., 2018a, A&A, 616, 1
Bryson S. T. et al., 2013, PASP, 125, 889
Buccino A. P., Lemarchand G. A., Mauas P. J. D., 2007, Icarus, 192, 582
Caramazza M., Flaccomio E., Micela G., Reale F., Wolk S. J., Feigelson E. D., 2007, A&A, 471, 645
Carrington R. C., 1859, MNRAS, 20, 13
Choi J., Dotter A., Conroy C., Cantiello M., Paxton B., Johnson B. D., 2016, ApJ, 823, 102
Cho I-H., Cho K-S., Nakariakov V. M., Kim S., Kumar P., 2016, ApJ, 830, 110
Cutri R. M. et al., 2014, VizieR Online Data Catalog, 2328
Davenport J. R. A., 2016, ApJ, 829, 23
Davenport J. R. A. et al., 2014, ApJ, 797, 122
de la Reza R., Pinzón G., 2004, AJ, 128, 1812
Dolla L. et al., 2012, ApJ, 749, L16
Dopita M., Hart J., McGregor P., Oates P., Bloxham G., Jones D., 2007, Ap&SS, 310, 255
Dotter A., 2016, ApJS, 222, 8
Doyle J. G. et al., 2018, MNRAS, 475, 2842
Edwin P. M., Roberts B., 1983, Sol. Phys., 88, 179
Favata F., Flaccomio E., Reale F., Micela G., Sciortino S., Shang H., Stassun K. G., Feigelson E. D., 2005, ApJS, 160, 469
Feigelson E. D., 2010, Proceedings of the National Academy of Science, 107, 7153
Flaccomio E., Micela G., Sciortino S., Cody A. M., Guarcello M. G., Morales-Calderòn M., Rebull L., Stauffer J. R., 2018, A&A, in press (arXiv:1807.08525)
Gilliland R. L. et al., 2010, ApJ, 713, L160
Gizis J. E., Paudel R. R., Mullan D., Schmidt S. J., Burgasser A. J., Williams P. K. G., 2017, ApJ, 845, 33
Goddard C. R., Nisticò G., Nakariakov V. M., Zimovets I. V., 2016, A&A, 585, A137
Gruber D. et al., 2011, A&A, 533, A61
Günther M. N. et al., 2017, MNRAS, 472, 295
Hawley S. L., Fisher G. H., 1992, ApJS, 78, 565
Hawley S. L., Davenport J. R. A., Kowalski A. F., Wisniewski J. P., Hebb L., Deitrick R., Hilton E. J., 2014, ApJ, 797, 121
Heyner D., Glassmeier K.-H., Schmitt D., 2012, ApJ, 750, 133
Hilton E. J., 2011, PhD thesis, University of Washington
Houdebine E. R., Mullan D. J., 2015, ApJ, 801, 106
Houdebine E. R., Mullan D. J., Bercu B., Paletou F., Gebran M., 2017, ApJ, 837, 96
Huber D. et al., 2014, ApJS, 211, 2
Ilgner M., Nelson R. P., 2006, A&A, 455, 731
Inglis A. R., Nakariakov V. M., 2009, A&A, 493, 259
Inglis A. R., Ireland J., Dennis B. R., Hayes L., Gallagher P., 2016, ApJ, 833, 284
Jackman J. A. G. et al., 2018, MNRAS, 477, 4655
Jansen F. et al., 2001, A&A, 365, L1
Johnstone C. P., Gregory S. G., Jardine M. M., Getman K. V., 2012, MNRAS, 419, 29
Kalberla P. M. W., Burton W. B., Hartmann D., Arnal E. M., Bajaja E., Morras R., Pöppel W. G. L., 2005, A&A, 440, 775
Kay C., Opher M., Kornbleuth M., 2016, ApJ, 826, 195
Kolotkov D. Y., Nakariakov V. M., Kupriyanova E. G., Ratcliffe H., Shibasaki K., 2015, A&A, 574, A53
Kolotkov D. Y., Anfinogentov S. A., Nakariakov V. M., 2016, A&A, 592, A153
Kowalski A. F., Hawley S. L., Holtzman J. A., Wisniewski J. P., Hilton E. J., 2010, ApJ, 714, L98
Kowalski A. F., Hawley S. L., Wisniewski J. P., Osten R. A., Hilton E. J., Holtzman J. A., Schmidt S. J., Davenport J. R. A., 2013, ApJS, 207, 15
Kulkarni S. R., Rau A., 2006, ApJ, 644, L63
Kumar P., Nakariakov V. M., Cho K-S., 2017, ApJ, 836, 121
Kupriyanova E. G., Melnikov V. F., Nakariakov V. M., Shibasaki K., 2010, Sol. Phys., 267, 329
Lacy C. H., Moffett T. J., Evans D. S., 1976, ApJS, 30, 85
Laming J. M., 2015, Living Reviews in Solar Physics, 12, 2
Lammer H. et al., 2007, Astrobiology, 7, 185
Lingam M., Loeb A., 2017, ApJ, 848, 41
López-Santiago J., Crespo-Chacón I., Micela G., Reale F., 2010, ApJ, 712, 78
McCormac J., Pollacco D., Skillen I., Faedi F., Todd I., Watson C. A., 2013, PASP, 125, 548
McLaughlin J. A., Thurgood J. O., MacTaggart D., 2012, A&A, 548, A98
McLaughlin J. A., Nakariakov V. M., Dominique M., Jelínek P., Takasao S., 2018, Space Sci. Rev., 214

Mann A. W., Feiden G. A., Gaidos E., Boyajian T., von Braun K., 2015, ApJ, 804, 64
Mathioudakis M., Seiradakis J. H., Williams D. R., Avgoloupis S., Bloomfield D. S., McAteer R. T. J., 2003, A&A, 403, 1101
Mitra-Kraev U., Harra L. K., Williams D. R., Kraev E., 2005, A&A, 436, 1041
Moffett T. J., 1974, ApJS, 29, 1
Moon Y.J., Choe G. S., Park Y. D., Wang H., Gallagher P. T., Chae J., Yun H. S., Goode P. R., 2002, ApJ, 574, 434
Mullan D. J., Mathioudakis M., Bloomfield D. S., Christian D. J., 2006, ApJS, 164, 173
Murphy S. J., Lawson W. A., 2015, MNRAS, 447, 1267
Murray M. J., van Driel-Gesztelyi L., Baker D., 2009, A&A, 494, 329
Nakamoto T., Hayashi M. R., Kita N. T., Tachibana S., 2005, in Krot A. N., Scott E. R. D., Reipurth B., eds, ASP Conf. Ser. Vol. 341, Chondrites and the Protoplanetary Disk, Astron. Soc. Pac., San Francisco, p. 883
Nakariakov V. M., Melnikov V. F., 2009a, Space Sci. Rev., 149, 119
Nakariakov V. M., Melnikov V. F., 2009b, Space Sci. Rev., 149, 119
Nakariakov V. M., Ofman L., 2001, A&A, 372, L53
Nakariakov V. M., Arber T. D., Ault C. E., Katsiyannis A. C., Williams D. R., Keenan F. P., 2004, MNRAS, 349, 705
Nakariakov V. M., Foullon C., Verwichte E., Young N. P., 2006, A&A, 452, 343
Nakariakov V. M. et al., 2016, Space Sci. Rev., 200, 75
Nisticò G., Pascoe D. J., Nakariakov V. M., 2014, A&A, 569, A12
Ofman L., Wang T., 2002, ApJ, 580, L85
Ofman L., Wang T. J., 2008, A&A, 482, L9
Orlando S., Reale F., Peres G., Mignone A., 2011, MNRAS, 415, 3380
Osten R., Livio M., Lubow S., Pringle J. E., Soderblom D., Valenti J., 2013, ApJ, 765, L44
Osten R. A., Wolk S. J., 2015, ApJ, 809, 79
Pandey J. C., Srivastava A. K., 2009, ApJ, 697, L153
Paudel R. R., Gizis J. E., Mullan D. J., Schmidt S. J., Burgasser A. J., Williams P. K. G., Berger E., 2018, ApJ, 861, 76
Pecaut M. J., Mamajek E. E., 2013, ApJS, 208, 9
Pecaut M. J., Mamajek E. E., 2016, MNRAS, 461, 794
Prusti T. et al.(Gaia Collaboration), 2016, A&A, 595, A1
Pugh C. E., Armstrong D. J., Nakariakov V. M., Broomhall A.-M., 2016, MNRAS, 459, 3659
Pugh C. E., Broomhall A.-M., Nakariakov V. M., 2017, A&A, 602, A47
Ramsay G., Doyle J. G., 2015, MNRAS, 449, 3015
Ranjan S., Wordsworth R., Sasselov D. D., 2017, ApJ, 843, 110
Rimmer P. B., Xu J., Thompson S., Gillen E., Sutherland J., Queloz D., 2018, Science Advances, 4, eear3302
Roberts B., Edwin P. M., Benz A. O., 1984, ApJ, 279, 857
Robitaille T. P. et al., 2013, A&A, 558, A33
Schmidt S. J. et al., 2016, ApJ, 828, L22
Segura A., Walkowicz L. M., Meadows V., Kasting J., Hawley S., 2010, Astrobiology, 10, 751
Selwa M., Murawski K., Solanki S. K., 2005, A&A, 436, 701
Shibayama T. et al., 2013, ApJS, 209, 5
Shu F. H., Shang H., Gounelle M., Glassgold A. E., Lee T., 2001, ApJ, 548, 1029
Simões P. J. A., Hudson H. S., Fletcher L., 2015, Sol. Phys., 290, 3625
Skrutskie M. F. et al., 2006, AJ, 131, 1163
Smith R. K., Brickhouse N. S., Liedahl D. A., Raymond J. C., 2001, ApJ, 556, L91
Stassun K. G., Ardila D. R., Barsony M., Basri G., Mathieu R. D., 2004, AJ, 127, 3537
Thurgood J. O., Pontin D. I., McLaughlin J. A., 2017, ApJ, 844, 2
Tsurutani B. T., Gonzalez W. D., Lakhina G. S., Alex S., 2003, Journal of Geophysical Research: Space Physics, 108, n/a
Van Doorsselaere T., De Groof A., Zender J., Berghmans D., Goossens M., 2011, ApJ, 740, 90
Van Doorsselaere T., Kupriyanova E. G., Yuan D., 2016, Sol. Phys., 291, 3143
VanderPlas J. T., 2018, ApJS, 236, 16
Vaughan S., 2005, A&A, 431, 391
Venot O., Rocchetto M., Carl S., Roshni Hashim A., Decin L., 2016, ApJ, 830, 77
Vida K., Kővári Z., Pál A., Oláh K., Kriskovics L., 2017, ApJ, 841, 124
Wang T., 2011, Space Sci. Rev., 158, 397
Welsh B. Y. et al., 2006, A&A, 458, 921
Wheatley P. J. et al., 2018, MNRAS, 475, 4476
Wilms J., Allen A., McCray R., 2000, ApJ, 542, 914
Wolf C. et al., 2018, PASA, 35, e010
Wood B. E., Linsky J. L., 2010, ApJ, 717, 1279
Wood B. E., Laming J. M., Karovska M., 2012, ApJ, 753, 76
Wu C-J., Ip W-H., Huang L-C., 2015, ApJ, 798, 92
Yang H. et al., 2017, ApJ, 849, 36
Zaitsev V. V., Stepanov A. V., 2008, Phys. Usp., 51, 1123
Zaitsev V. V., Kislyakov A. G., Stepanov A. V., Kliem B., Furst E., 2004, Astron. Lett., 30, 319
Zhilyaev B. E. et al., 2000, A&A, 364, 641
Zimovets I. V., Nakariakov V. M., 2015, A&A, 577, A4

This paper has been typeset from a TEX/LATEX file prepared by the author.